Inhibition of photocorrosion of CdS via assembling with thin film TiO$_2$ and removing formed oxygen by artificial gill for visible light overall water splitting

Xiaofeng Ning [a,b], Jian Li [c], Baojun Yang [a], Wenlong Zhen [a], Zhen Li [a], Bin Tian [a], Gongxuan Lu [a,*]

[a] State Key Laboratory for Oxo Synthesis and Selective Oxidation, Lanzhou Institute of Chemical Physics, Chinese Academy of Science, Lanzhou 730000, China
[b] University of Chinese Academy of Science, Beijing 100049, China
[c] China Astronaut Research and Training Center, Beijing 100094, China

ABSTRACT

CdS is a well-known and important visible-light responsive photocatalyst for overall water splitting. However, the serious photocorrosion property limits its application in photocatalysis. Through modification TiO$_2$ thin film over CdS surface, TiO$_2$/CdS photocatalyst exhibited an obviously enhanced photocatalytic stability. The H$_2$ evolution rate (3.074 μmol h^{-1} g^{-1}) of modified Pt-TiO$_2$/CdS under visible light toward overall water splitting was almost 6 times higher than that of CdS sample (0.534 μmol h^{-1} g^{-1}). The application of artificial gill in photocatalytic overall water splitting system removed the newly formed oxygen from catalyst surface mainly inhibiting the hydrogen and oxygen back recombination to water and preventing the oxygen led oxidation or photocorrosion. By these two strategies, we fulfilled visible light induced overall water splitting in CdS dispersion and achieved satisfied stability during reaction.
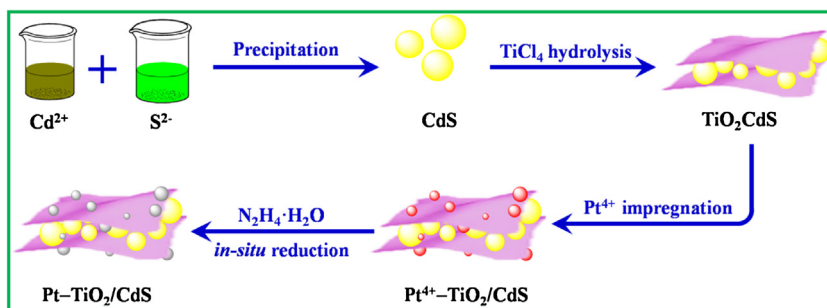
© 2017 Elsevier B.V. All rights reserved.

1. Introduction

The replacement of fossil fuel by renewable solar energy has attracted extensive attention recently, among the several options, the hydrogen evolution driven by solar energy is known as one of promising ways. Photocatalytic overall water splitting can generate hydrogen and oxygen simultaneously in semiconductor dispersion [1–21]. A variety of photocatalysts consisting of metal cations with d^0 or d^{10} electronic configurations were reported active for this reaction [22–26]. However, on the one hand, most of developed photocatalysts for splitting water are only responsive to ultraviolet light which accounts for only 4% of solar radiation over the Earth. Although many visible-light driven photocatalysts, such as oxides [27–31], oxynitrides [32–35] and sulfides [36–43] and polymers [44–55], were reported to active for hydrogen generation, CdS is still one of excellent candidates for water splitting because of its narrow band gap (ca. 2.4 eV) and suitable conduction band and valence band both for hydrogen and oxygen formation. On the other hand, semiconductors sensitive to visible light are easy to be

photocorroded. Such photocorrosion seriously impeded its application in photocatalysis [56,57], in which the S^{2-} in CdS is prone to be oxidized by photogenerated holes accompanied by leaching of the toxic cadmium ions (Cd^{2+}) [58–61]. If the anti-photocorrosion film is fabricated over CdS surface, the photogenrated hole oxidation of CdS can not take place, and the hole is going to oxidize water to oxygen instead. There were some papers published related to stabilization of CdS, for example, Zhang et al. found that the anti-photocorrosion of CdS could be achieved by PdS-cocatalyst modification [62]. Su et al. reported that the PANI@CdS core-shell nanospheres exhibited enhanced anti-photocorrosion properties and photocatalytic hydrogen production activity [63]. Hu et al. investigated that carbon-coating over CdS could protect the CdS from photocorrosion [64]. Feng et al. constructed core-shell type concentric CdS NR phase junctions composed of hexagonal core and cubic shell towards photocatalytic H$_2$ production with long-time stability [65]. Du et al. constructed a Ni$_2$P-1D CdS NR system towards for photocatalytic H$_2$ evolution, which was active for H$_2$ evolution with good stability [66]. In fact, the photocorrosion is not only related to the photogenerated hole in semiconductor itself, but also related to the newly formed oxygen in the water. Maybe another ignored factor is the higher solubility of oxygen in water than hydrogen, which leads to more seriously photocorrosion of

* Corresponding author.
E-mail address: gxlu@lzb.ac.cn (G. Lu).

Scheme 1. Schematic illustration on the synthesis of Pt-TiO$_2$/CdS sample.

CdS enhanced by newly formed oxygen. Such high concentration of oxygen in water also enhance the reverse recombination reaction of hydrogen and oxygen which further impede the efficiency of water splitting in semiconductor dispersion [67,68].

In this paper, we modified CdS surface with TiO$_2$ film, and found that this film could improve the stability of CdS significantly during water splitting reaction. In addition, we apply artificial gill to remove newly formed O$_2$ from water to prevent the oxygen leading photocorrosion and to inhibit the hydrogen and oxygen recombination back to water. By these two strategies, we fulfilled visible light induced overall water splitting by CdS and achieved satisfied stability during reaction. This work may provide new insight for the development of highly stable and efficient photocatalysts in sulfide semiconductor dispersion for hydrogen production.

2. Experimental section

2.1. Materials

All chemicals were commercial purchased and used without further purification. Cadmium nitrate (Cd(NO$_3$)$_2$·4H$_2$O, Tianjin Kemiou Chemical Reagent Co., Ltd, AR, ≥99.0%), sodium sulfide (Na$_2$S·9H$_2$O, Chengdu Kelong Chemical Reagent Co., Ltd, AR, ≥98.0%), titanium tetrachloride (TiCl$_4$, Tianjin Kemiou Chemical Reagent Co., Ltd, AR, ≥99.0%), chloroplatinic acid, (H$_2$PtCl$_6$·6H$_2$O, Tianjin Kemiou Chemical Reagent Co., Ltd, AR, ≥99.0%), hydrazine hydrate (H$_4$N$_2$·H$_2$O, Xilong Chemical Co., Ltd., AR, >80%), sodium sulfate (Na$_2$SO$_4$, Xilong Chemical Co., Ltd., AR, >99%), deuteroxide (D$_2$O, J&K Scientific Ltd., AR, >99%) and heaven-oxygen water (H$_2$^{18}O, J&K Scientific Ltd., AR, >97%). All of the reagents were used in the experiments without further purification. Deionized water was used in the synthesis and reaction.

2.2. Preparation of CdS sample

CdS sample was prepared by a typical precipitation method. Briefly, 1.07 g Cd(NO$_3$)$_2$·4H$_2$O was dissolved in 150 mL of deionized water and stirred vigorously for 30 min, 1.67 g Na$_2$S·9H$_2$O was dissolved into another 50 mL of deionized water by ultrasonication to obtain the Na$_2$S solution. Then the Na$_2$S solution was slowly added into the above-mentioned Cd(NO$_3$)$_2$ solution in a drop-by-drop process under vigorous stirring. After stirring for 3 h, the obtained yellow precipitate was filtrated, washed with deionized water several times, and dried at 80 °C for 12 h. Finally, the products were collected and ground into powder by an agate mortar.

2.3. Preparation of TiO$_2$-modified CdS photocatalyst

The TiO$_2$-modified CdS photocatalyst was prepared by an impregnation method via the hydrolysis of TiCl$_4$. In a typical preparation, 0.25 g CdS was uniformly dispersed into 100 mL of distilled water under constant magnetic stirring. Subsequently, a known amount of TiCl$_4$ solution was injected into the above suspension. After stirring for 2 h, the resulting sample was filtrated, rinsed with deionized water, and dried at 80 °C to obtain the TiO$_2$/CdS photocatalysts. To further investigate the effect of TiO$_2$ content on the photocatalytic performance of the CdS photocatalyst, the amount of TiO$_2$ (the weight ratio of Ti to CdS) was controlled to be 0, 0.1, 0.2, 0.3, 0.5 and 1.0 wt% respectively, and the resultant TiO$_2$/CdS samples were referred as CdS, (0.1 wt%) TiO$_2$/CdS, (0.2 wt%) TiO$_2$/CdS, (0.3 wt%) TiO$_2$/CdS, (0.5 wt%) TiO$_2$/CdS and (1.0 wt%) TiO$_2$/CdS, respectively.

2.4. Preparation of Pt-TiO$_2$/CdS photocatalyst

The platinization of Pt-TiO$_2$/CdS was prepared by a typical hydrazine hydrate reduction method (as shown in Scheme 1). 0.25 g as-prepared TiO$_2$/CdS sample with a known amount of H$_2$PtCl$_6$ solution was stirred in half an hour, then hydrazine hydrate was dropped into the solution. Finally, the products were filtrated, rinsed with deionized water, and dried at 80 °C to obtain the Pt-TiO$_2$/CdS photocatalysts. The amount of Pt (the weight ratio of Pt to TiO$_2$/CdS) was controlled to be 0.1, 0.5, 1.0, 2.0, and 3.0 wt%, and the resultant Pt/TiO$_2$/CdS samples were referred to as, 0.1% Pt-TiO$_2$/CdS, 0.5% Pt-TiO$_2$/CdS, 1.0% Pt-TiO$_2$/CdS, 2.0% Pt- TiO$_2$/CdS and 3.0% Pt-TiO$_2$/CdS, respectively.

2.5. Characterization of the catalysts

The powder X-ray diffraction patterns (XRD) of the samples were recorded on a Rigaku B/Max-RB X-ray diffractometer with a nickel-filtrated Cu Kα radiation in the 2θ ranging from 10 to 60° and a position sensitive detector using a step size of 0.017° and a step time of 15 s at 40 mA and 40 kV. X-ray photoelectron spectroscopy (XPS) analysis was performed using a VG Scientific ESCALAB 250Xi-XPS photoelectron spectrometer with an Al Kα X-ray resource. The binding energies were calibrated by the C1s binding energy of 284.7 eV. The specific surface areas of the catalysts were determined by N$_2$ adsorption-desorption measurements by employing the Brunauer-Emmet-Teller (BET) method (Micromeritics apparatus ASAP 2020M) at 77 K. Transmission electron microscopy (TEM) and HRTEM images were taken with a Tecnai-G2-F30 field emission transmission electron microscope operating at accelerating voltage of 300 kV. Elemental mapping was performed by using an energy-dispersive X-ray spectrometer (EDS) attached to the TEM instrument. Ultraviolet-visible (UV–vis) diffuse reflectance spectra (DRS) were obtained with a Hewlett-Packard 8453 spectrophotometer in which BaSO$_4$ powder was used as the internal standard to obtain the optical properties of the samples. The photoluminescence (PL) spectra for samples were investigated on an Edinburgh FL/FS900 spectrophotometer with an excitation wave-length of 425 nm. The amount of Cd^{2+} in the reaction supernatant liquid resulting from photocorrosion was analysed by inductively coupled
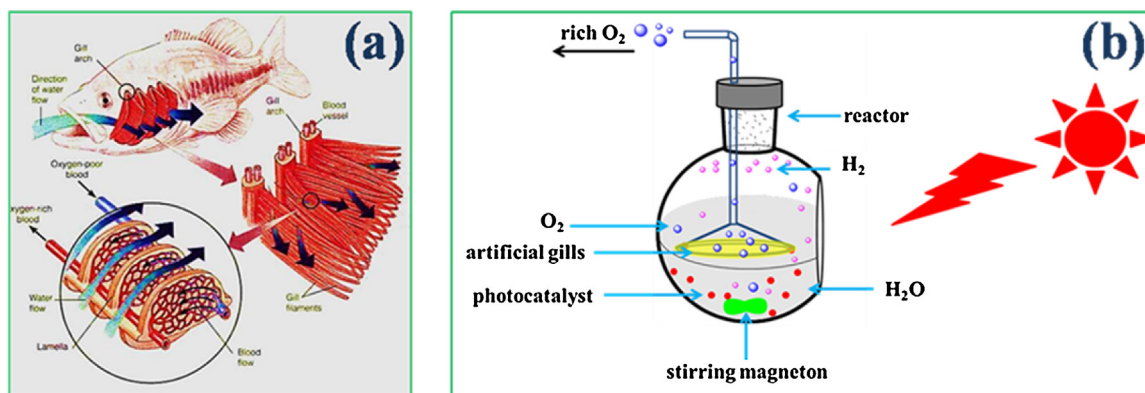
Fig. 1. (a): The structure of fish gill and (b) the schematic diagram of photocatalytic reaction system.

plasma-optical emission spectrometer (ICP, Agilent 725-ES) unit. The ICP signal intensities were calibrated by using a Cd elemental ICP standard solution.

2.6. Artificial gill

It is known that fish can extract the dissolved oxygen from the water through the gill in the water. The gill structure is shown in Fig. 1a. Gill is a typical respiratory organ of fish, which consists of gill arch, gill rake, gill filament, gill lamella, etc. Fish exchanges the gas by gill lamella in the water. Gill wall is very thin, and contains a lot of capillaries. In the gills, the dissolved oxygen in the water is first absorbed by the capillaries, and the carbon dioxide is exchanged into the water in the mean time. One can achieve similar function just using a gas diffusion polymer film, one side is water with dissolved oxygen and another side is bubbled with high pure argon gas. By this way, the oxygen concentration difference leads to oxygen diffusion from water side to the gas side, then the dissolved oxygen in water could be transferred from reaction mixture to gas phase. Actually this technique has been used to get oxygen from water, and the equipment is called artificial gill. We apply artificial gill to the photocatalytic overall water splitting system. The continuous argon gas was injected to decrease oxygen concentration in gas side of separation membrane, thus the dissolved oxygen would penetrate the separation membrane and moved out of the reaction system. Fig. 1b displays the schematic diagram of our artificial gill using in photocatalytic reaction.

2.7. Photocatalytic H_2 evolution activity

Photocatalytic experiments were performed at room temperature in a sealed Pyrex flask (212 mL) with a flat window (an efficient irradiation area of 9.8 cm^2) and a silicone rubber septum for sampling. 100 mg of catalyst was dispersed into 150 mL H_2O under the ultrasound treatment (25 kHz, 250 W) about 10 min. Prior to irradiation, the reactant mixture was degassed by bubbling Ar gas for 40 min. The Xenon lamp (HSX-UV 300, NBeT) with a 420 nm cut-off filter was used as a light source to trigger the photocatalytic reaction and was positioned 20 cm away from the reactor. The amount or rate of hydrogen evolution was measured using gas chromatograph (Aglient 6820, TCD, 13 X columns, Ar carrier). A continuous magnetic stirrer was applied at the bottom of the reactor in order to keep the photocatalyst in suspension status during the whole experiment.

The apparent quantum efficiency (AQE) was measured under the same photocatalytic reaction conditions with irradiation light through a bandpass filter (430, 460, 490, 520, or 550 nm). Photon flux of the incident light was determined using a Ray virtual radiation actinometer (FU 100, silicon ray detector, light spectrum, 400–700 nm; sensitivity, 10–50 μV μmol^{-1} m^{-2} s^{-1}). The reaction solutions were irradiated for 2 h with bandpass filters for AQE tests on the H_2 production. The following equation was used to calculate the AQE.

$$AQE = \frac{2 \times \text{the number of evolved hydrogen molecules}}{\text{the number of incident photos}} \times 100\%$$

The recycling test of photocatalytic H_2 evolution over the catalyst was done as follows. Typically, after the photocatalytic reaction of the first run under visible light irradiation, the photocatalytic system was thoroughly degassed again, without the separation of photocatalysts. Subsequently, the thoroughly degassed system was irradiated again by a 300 W Xe lamp with a 420 nm cut-off filter. Analogously, the following runs of photocatalytic recycling tests were performed.

2.8. Photocatalytic splitting D_2O and $H_2{}^{18}O$ isotope-labeled experiments

The isotopes tracer experiments have been performed under downsizing the experimental conditions of photocatalytic splitting H_2O. Typically, 10 mg catalyst dispersed in 10 mL D_2O or 1 mL $H_2{}^{18}O$ in the sealed Pyrex flask. After ultrasonic treatment for 30 min, the suspended aqueous solution is degassed by bubbling Ar gas for another 40 min. After visible light irradiation for 6 h, the gas mixture in container was measured by GC–MS (MAT 271). According to the NIST mass spectral database, the gas products were deduced from MS/MS mode and analyzed by scan mode.

2.9. Photoelectrochemical performance

All the electrochemical measurements were measured on an electrochemical analyzer (CHI660E) in a homemade standard three-electrode quartz cell consisting of an organic glass enclosure with a quartz window and a 1.2 cm diameter opening opposite the window to the work electrode was clamped. The working electrode was prepared by drop-coating sample suspensions directly onto the precleaned indium tin oxide glass (ITO glass) surface. Platinum plate was used as the counter electrode and a saturated calomel electrode (SCE) as the reference electrode. The electrolyte was 0.4 M aqueous Na_2SO_4 solution without any additives. The visible light irradiation source was a 300 W Xe arc lamp system equipped with a 420 nm cut-off filter. The surface area of the working electrode exposed to the electrolyte was about 0.95 cm^2. The cathodic polarization curves were obtained using the linear sweep voltammetry (LSV) technique with a scan rate of 1 mV/s.
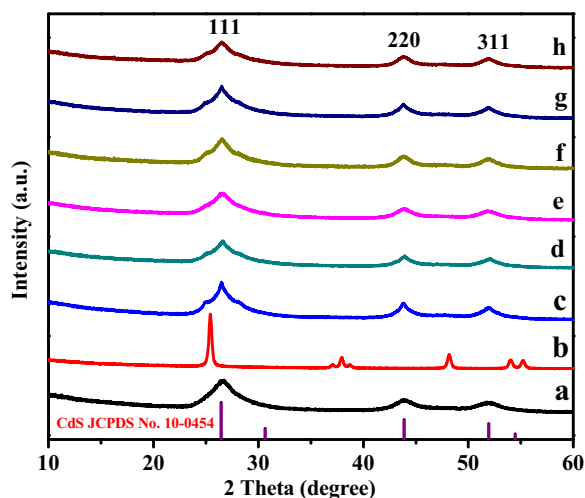
Fig. 2. XRD patterns of various samples: (a) CdS, (b) TiO$_2$, (c) TiO$_2$/CdS, (d) 0.1%Pt-TiO$_2$/CdS, (e) 0.5%Pt-TiO$_2$/CdS, (f) 1.0%Pt-TiO$_2$/CdS, (g) 2.0%Pt-TiO$_2$/CdS, and (h) 3.0%Pt-TiO$_2$/CdS.

Fig. 3. The UV–vis diffuse reflectance spectra (DRS) of the as-prepared samples; inset is the plot of transformed Kubelka–Munk function vs. the energy of light.

3. Results and discussion

3.1. XRD analysis

The crystal structures of the as-prepared pure CdS and Pt/CdS-TiO$_2$ photocatalysts with different Pt loading have been recorded by XRD technique (as shown in Fig. 2). It is clear that all the diffraction peaks of the homemade TiO$_x$ sample can be indexed to the anatase TiO$_2$ phase (JCPDS No. 65-5714). The strong peaks observed at 25.3, 27.8, 48.0, 53.9, 55.1, 62.7, 68.8, 70.3, and 75.0° can be ascribed to the (101), (004), (200), (105), (211), (204), (116), (220), and (215) planes of anatase phase, respectively [69]. Furthermore, no impurity peaks were detected in the TiO$_2$ sample, revealing the high purity of the as-synthesized products. It is clear that all the diffraction peaks of the CdS samples can be indexed to the cubic CdS phase (JCPDS No. 10-0454). The peaks of scattering angles (2θ values) located at ca. 26.5, 43.9 and 52.1° are attributed to the diffraction of the (111), (220) and (311) crystal planes of cubic CdS, respectively [70]. Because of the very limited amount and TiO$_2$ film was in well dispersion, therefore no diffraction peaks of TiO$_2$ and Pt nanoparticles can be observed in the XRD pattern. All the Pt-TiO$_2$/CdS samples show a similar diffraction peak with the pure CdS sample, indicating that the crystallization and crystallite size of CdS are not affected by the TiCl$_4$ hydrolysis processes owing to the mild conditions.

3.2. UV–vis diffuse reflection spectra

Fig. 3 shows the UV–vis DRS spectra of prepared CdS, TiO$_2$, TiO$_2$/CdS and the Pt-TiO$_2$/CdS samples. It is clearly shown that the TiO$_2$ sample only responds to UV light, which is in accordance with its wide band gap (ca. 3.2 eV). Pure CdS nanoparticles exhibit a strong and broad absorption in the visible light. After its surface modification with TiO$_2$ thin film, the resultant TiO$_2$/CdS photocatalyst shows an increased absorption in the visible light region, which mainly can be attributed to the d–d transition of Ti ions in the TiO$_2$ [71]. In addition, the interfacial charge transfer absorption from the VB of CdS to TiO$_2$ also possibly contributes to the enhanced visible light absorption [72]. Apparently, the band gap transition of TiO$_2$/CdS is not affected by the surface platinization, the sample Pt-TiO$_2$/CdS and TiO$_2$/CdS display a similar absorption curve, which may be due to the limited amount of Pt cocatalyst. Therefore, it indicates that the modification of Pt cocatalysts does not significantly affect the optical absorption feature of TiO$_2$/CdS
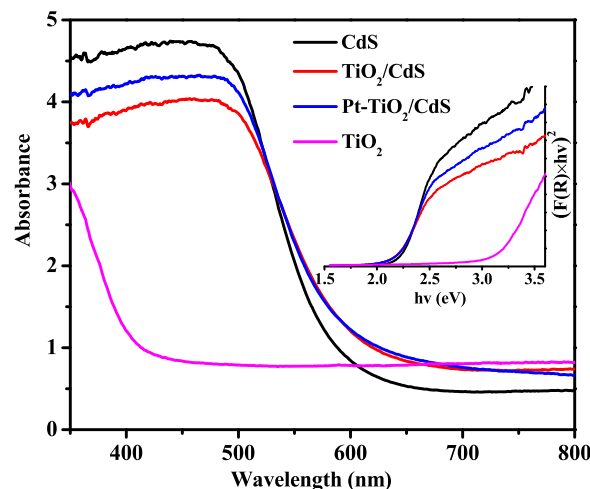
nanoparticle, which suggests that the deposition of Pt is a modification process rather than a lattice doping. Compared with pure CdS powder, the red shift phenomenon is observed over TiO$_2$/CdS and Pt-TiO$_2$/CdS catalysts, which is evidenced by the plot of transformed Kubelka–Munk function versus the energy of light [73].

As shown in the inset of Fig. 3, the band gaps of pure TiO$_2$, CdS, TiO$_2$/CdS and Pt-TiO$_2$/CdS are estimated to be ca. 3.2, 2.23, 2.19 and 2.19 eV, respectively. The variations of the band gap could probably make a different degree of delocalization and mobility of photoexcited electron and hole pairs, which might then lead to a different photocatalytic efficiency. Furthermore, the narrow band gap of sample suggests that it is able to be photoexcited to generate electron-hole pairs by visible light irradiation, thereby triggering chemical redox reactions.

3.3. Morphology analysis

Fig. 4 shows the SEM images of the CdS, TiO$_2$/CdS, Pt-TiO$_2$/CdS. It can be seen that CdS sample is composed of irregular particles with a size range of 20–70 nm due to a simple precipitation method, and the particle surface is smooth (Fig. 4A). After CdS coated with TiO$_2$ cocatalyst, the obtained TiO$_2$/CdS (Fig. 4B) showed the surface of CdS was uniformly covered by TiO$_2$ layer. After TiO$_2$/CdS was deposited by metal nanoparticle Pt (Fig. 4C), the sample morphology did not change significantly and was similar to the TiO$_2$/CdS sample, partially due to a very low amount of Pt cocatalyst loading and the small size of nanoparticle.

To further study the effects of modification TiO$_2$ and Pt on CdS morphology, TEM was performed. CdS was comprised of nanoparticle with irregular shape (Fig. S1a, Supporting Information). A set of crystal lattice fringes with a d spacing of 0.336 nm is disclosed in the HRTEM image (see Fig. S1b), which can be ascribed to the (111) planes of cubic CdS. After CdS surface is modified with TiO$_2$ thin film (Ti/CdS = 0.3 wt%), a misty thin film was coated on CdS surface in Fig. S1c. To confirm the components of TiO$_2$/CdS, the mapping analysis was performed and the corresponding results were shown in Fig.S1e, f. The elemental mapping of TiO$_2$/CdS clearly indicated that the distribution of Ti, Cd, S and O elements was relatively homogeneous in TiO$_2$/CdS.

Fig. 5a and b showed the Pt nanoparticles were uniformly distributed on the surface of CdS, and the lattice spacing of 0.229 nm was assigned to the (111) plane of Pt nanoparticles over Pt-TiO$_2$/CdS. The elemental mapping image (Fig. 5c, d) and EDS (Fig. 5e) showed that the photocatalyst contained S, Cd, Ti, O and Pt elements and their distribution were relatively homogeneous in CdS
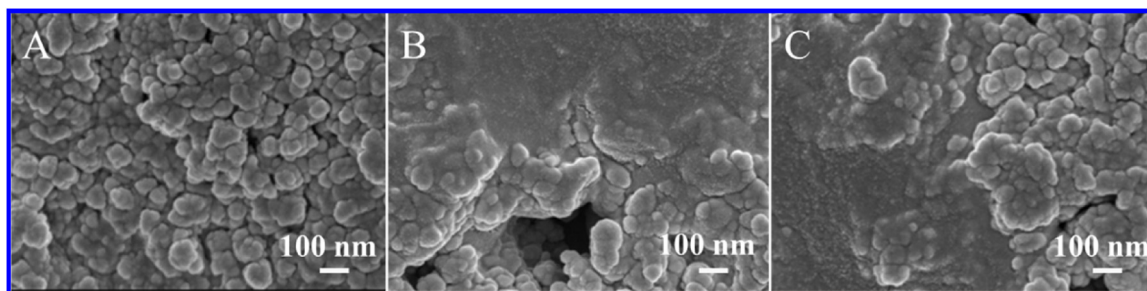
Fig. 4. SEM images of various samples: (A) CdS, (B) TiO_2/CdS, (C) Pt-TiO_2/CdS.

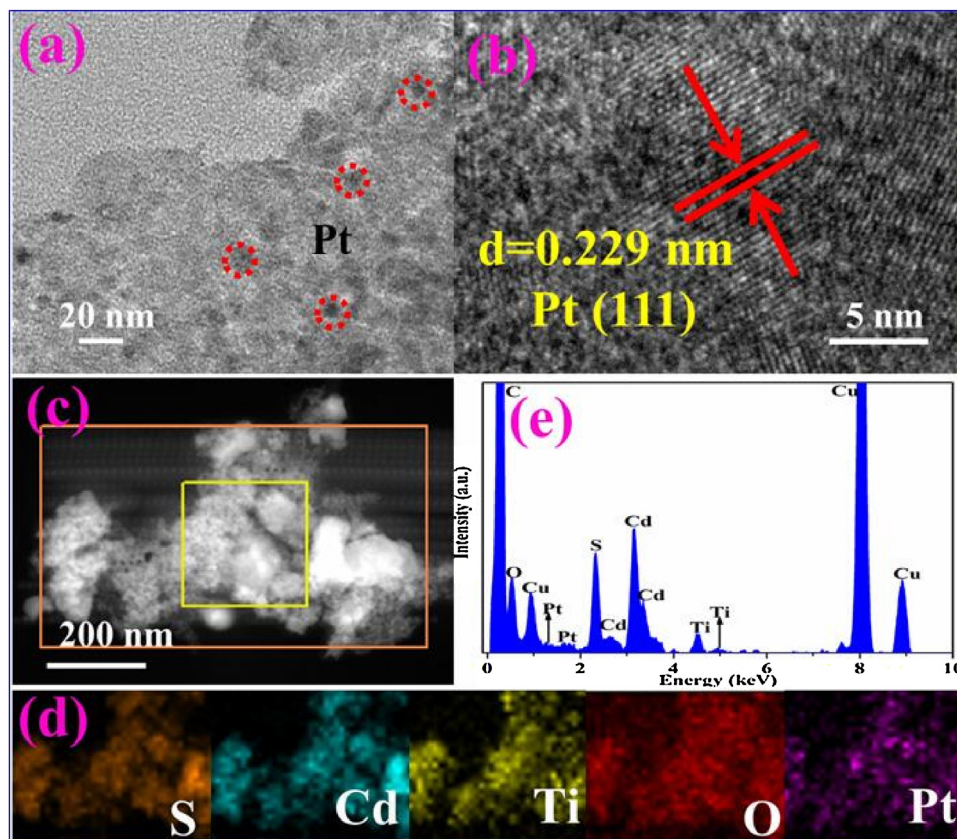**Fig. 5.** (a) The TEM images, (b) HRTEM image, (c) and (d) elemental mapping images, and (e) EDS analysis of Pt-TiO_2/CdS photocatalyst.

sample, which also proved that the Pt nanoparticles were uniformly dispersed on the surface of TiO_2/CdS.

3.4. BET surface areas and pore size distributions

In order to examine the specific surface area (S_{BET}) and pore-size distribution of the photocatalysts, BET (Brunauer-Emmett-Teller) gas-sorption measurements were carried out at 77 K. Fig. 6a shows the N_2 adsorption/desorption isotherms for the as-prepared samples. Based on the BDDT (Brunauer-Deming-Deming-Teller) classification, the isotherms of samples are identified as IV type, which is characteristic of mesoporous materials [74]. It is clear that CdS sample has two hysteresis loops, indicating bimodal pore-size distributions. The isotherm with a broad hysteresis loops at low relative pressure between 0.4 and 0.9, the hysteresis loop is of H2 type, which corresponds to ink-bottle pores. At relative high pressure range ($0.9 < P/P_0 < 1.0$), the shape of the hysteresis loop is of H3 type, implying the formation of slitlike pores that are generally associated with aggregates of platelike particles [75]. Furthermore,

the isotherm exhibits high adsorption at relative high pressure (P/P_0) range (approaching 1), suggesting the existence of macropores [76]. However, the isotherm of the TiO_2/CdS sample is slightly different from pure CdS, implying a variation of pore structures. First, the isotherm no longer exhibits high adsorption at high P/P_0 range (approaching 1), which suggests that the macropores are at least partially destroyed. Second, the hysteresis loop is of H3 type, also implying the formation of slitlike pores that are generally associated with aggregates of platelike particles [75]. The isotherm corresponding to Pt-TiO_2/CdS sample remains virtually unchanged as TiO_2/CdS (in Fig. 6a), indicating the retention of a similar pore structure after slight Pt incorporation.

The corresponding pore size distribution is shown in Fig. 6b. Generally, the as-prepared pure CdS sample exhibits a bimodal pore size distribution in the mesoporous region. The distribution is a relatively wide, pore-size from 2 to 10 nm, which will provide efficient transport pathways for reactant and product molecules [77]. Based on the previous reports [76], a bimodal mesopore size distribution is due to two different aggregates in the powders.
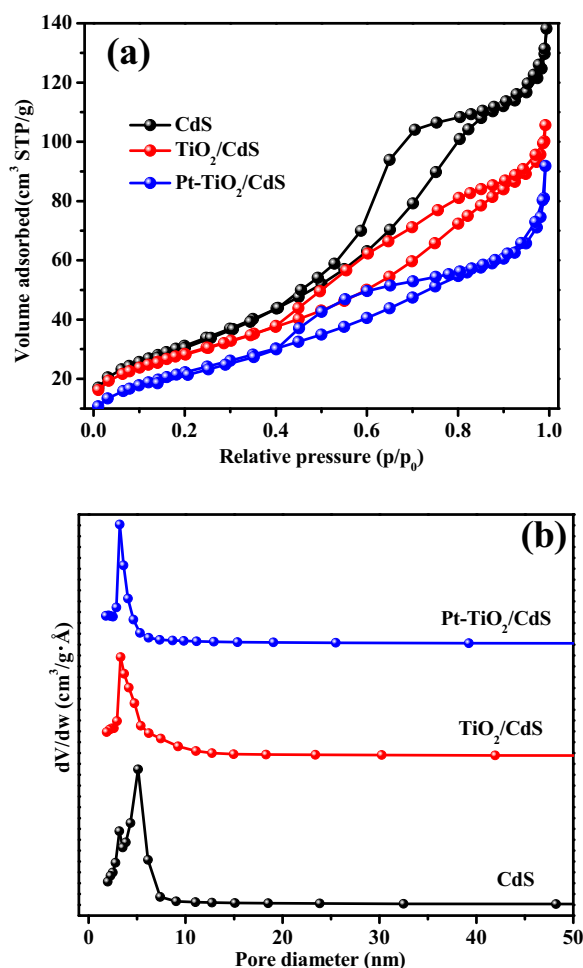
Fig. 6. (a) Nitrogen adsorption-desorption isotherms and (b) their corresponding pore size distribution curves of samples.

The smaller mesopores are usually related to primary intraagglomeration, while the larger ones are associated with secondary interaggregation. The pore-size distribution of TiO_2/CdS and Pt-TiO_2/CdS are also similar, about 2–5 nm. The quantitative details about the BET surface area, pore volume, and average pore size of as-prepared samples are presented in Table 1. Overall, the samples show a decrease in BET surface area, pore volume and average pore size after modifying TiO_2 and Pt nanoparticle. The result may be due to the TiO_2 and Pt were covered with the surface of CdS, which would block some pores of CdS, leading to the small BET surface area, pore volume and average pore size.

Generally, larger specific surface area usually contributes to highly efficient catalytic activity [76–78]. The larger specific surface area provides more surface active sites for the adsorption of reactants molecules, and makes the photocatalytic action more efficiently.

Table 1
Physicochemical Property of As-Prepared Samples.

Samples	S_{BET} $(m^2 g^{-1})^a$	Pore volume $(cm^3 g^{-1})^b$	Average pore size $(nm)^b$
CdS	114.72	0.188	6.55
TiO_2/CdS	103.83	0.144	5.55
Pt-TiO_2/CdS	83.69	0.110	5.25

[a] Obtained from BET method.
[b] Total pore volume taken from the nitrogen adsorption volume at a relative pressure (P/P_0) of 0.99.
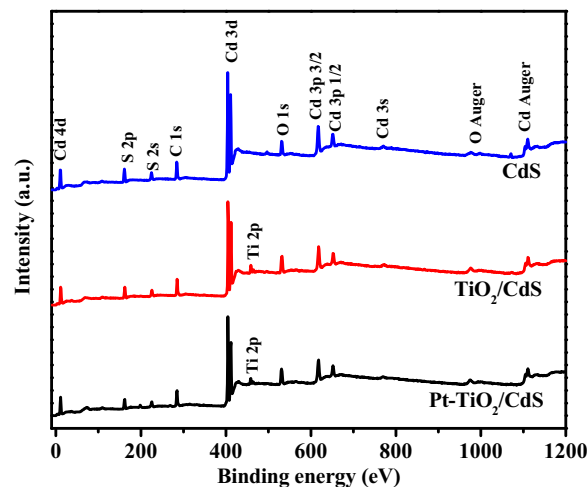

Fig. 7. Full XPS spectra of pure CdS, TiO_2/CdS and Pt-TiO_2/CdS.

3.5. XPS analyses

To further demonstrate the loading of TiO_2 and Pt cocatalyst on the surface of CdS sample and to investigate the chemical status of the as-synthesized samples, XPS analysis was carried out. Fig. 7 shows the XPS survey spectra for various samples, Fig. 8a and 8b present the high-resolution spectra of the Cd 3d and S 2p regions, respectively. The binding energies 405.0 and 411.8 eV correspond to Cd $3d_{5/2}$ and $3d_{3/2}$, respectively, indicating Cd^{2+} in CdS. The 6.8 eV difference between the binding energies of Cd $3d_{5/2}$ and Cd $3d_{3/2}$ peaks is also characteristic of Cd^{2+} states [79,80]. In addition, as shown in Fig. 8b, the binding energies of S 2p for S $2p_{3/2}$ and S $2p_{1/2}$ were determined to be about 161.4 and 162.6 eV, respectively, demonstrating S^{2-} in the CdS sample [81]. Compared with the binding energies both of S 2p and Cd 3d in pure CdS, Pt-TiO_2/CdS samples have a slightly up shift. The shift of binding energies may be attributed to the strong interactions between CdS nanoparticles and TiO_2 and Pt nanoparticles [82,83]. It is clear that TiO_2/CdS and Pt-TiO_2/CdS samples show Ti 2p peaks in Fig. 8c. The peaks located at around 458.9 eV and 464.6 eV corresponding to Ti $2p_{3/2}$ and Ti $2p_{1/2}$ respectively, which are typically peaks assigned to Ti^{4+} [84,85]. In Fig. 8d, the two main peaks emerging at binding energies of 71.1 and 74.4 eV were associated with Pt $4f_{7/2}$ and Pt $4f_{5/2}$, respectively, indicating that the Pt precursors could be reduced to metallic Pt by hydrazine hydrate reduction at room temperature. Evidently, the splitting value of 3.3 eV between these two bands is characteristic of the metallic Pt species.

3.6. Photocatalytic activity

The photocatalytic overall water splitting performances of photocatalysts are evaluated under visible light ($\lambda \geq 420$ nm) irradiation in a reactor equipped with an artificial gill, which can remove the oxygen dissolved in the dispersion out of the reactor. The blank tests indicated that no H_2 was produced in the absence of photocatalysts or without irradiation, suggesting that the evolution of H_2 was triggered by a photocatalytic process. Fig. 9a shows the photocatalytic H_2 production rate over various TiO_2/CdS samples. It can be seen that all the TiO_2/CdS samples exhibit higher photocatalytic activities than the CdS sample itself, and the (0.3 wt%)TiO_2/CdS photocatalyst shows the highest photocatalytic activity. The photocatalytic activity was gradually improved upon increasing the weight ratio of TiO_2 from 0 to 0.3 wt%, and then decreased with further increase of the molar ratio to 1.0. The decrease in activity may be caused by the light shielding effect of TiO_2 [86]. Due to the
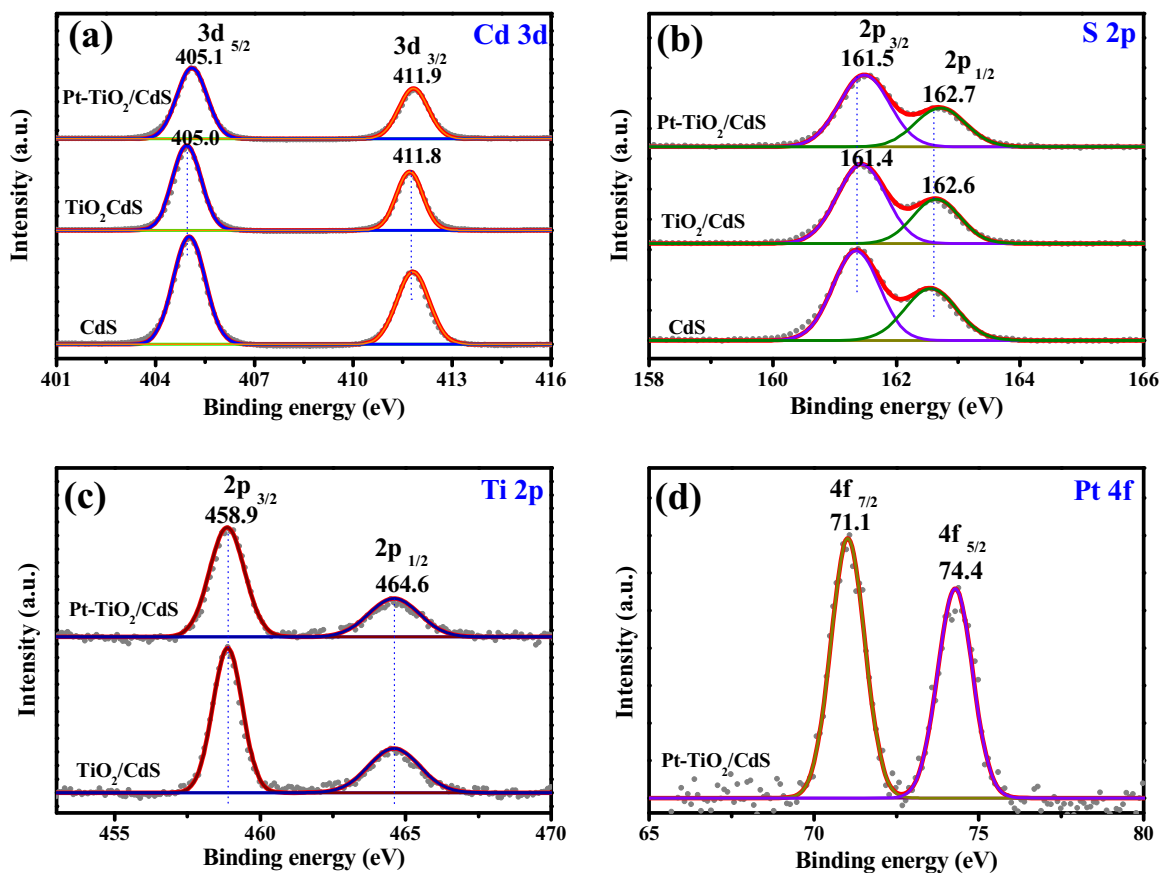
Fig. 8. The high resolution XPS spectra of (a) Cd3d, (b) S 2p, (c)Ti 2p and (d) Pt 4f high resolution XPS spectrum of prepared samples.
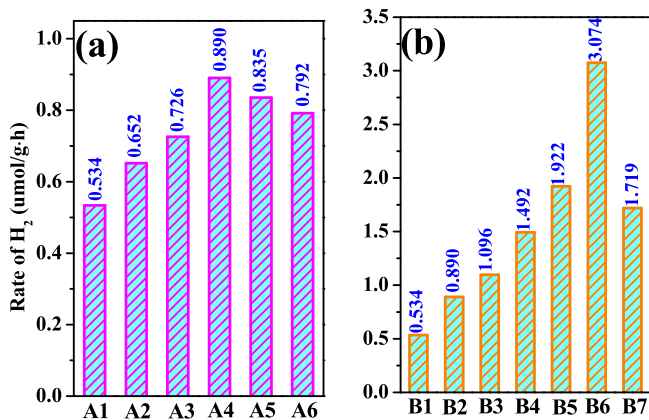

Fig. 9. Comparison of the photocatalytic splitting pure H_2O activity under visible light irradiation for various (a) TiO_2/CdS samples: (A1) CdS, (A2) (0.1 wt%)TiO_2/CdS, (A3) (0.2 wt%)TiO_2/CdS, (A4) (0.3 wt%)TiO_2/CdS, (A5) (0.5 wt%)TiO_2/CdS and (A6) (1.0 wt%)TiO_2/CdS, (b) various Pt loading on (0.3 wt%)TiO_2/CdS samples, (B1) CdS, (B2) (0.3 wt%)TiO_2/CdS, (B3) 0.1% Pt-TiO_2/CdS, (B4) 0.5% Pt-TiO_2/CdS, (B5)1.0% Pt-TiO_2/CdS, (B6) 2.0% Pt-TiO_2/CdS and (B7) 3.0% Pt-TiO_2/CdS.

Fig. 10. Cycling runs of the photocatalytic activity for various samples: (a) CdS, (b) TiO_2/CdS, (c) Pt-TiO_2/CdS without artificial gill photocatalytic system and (d) Pt-TiO_2/CdS.

excessive TiO_2 covering of the photoactive sites, it will result in a low generation of photoinduced charge carriers. Fig. 9b displays the activities of different Pt loading of Pt-TiO_2/CdS samples for the overall water splitting under visible light irradiation. It is shown that the sample loaded with 2.0% Pt possessed the highest H_2 evolution activity and the rate of H_2 formation (3.074 $\mu mol\,h^{-1}\,g^{-1}$), which was almost 6 times higher than that of CdS sample (0.534 umol $h^{-1}\,g^{-1}$). A decay of the rate was observed with further increasing the Pt loading amount to 3.0 wt%. It may be caused by the light shielding effect of excessive Pt [86]. All of the Pt-TiO_2/CdS samples
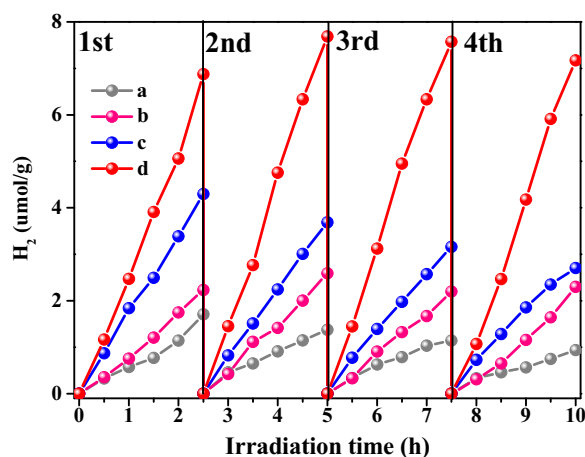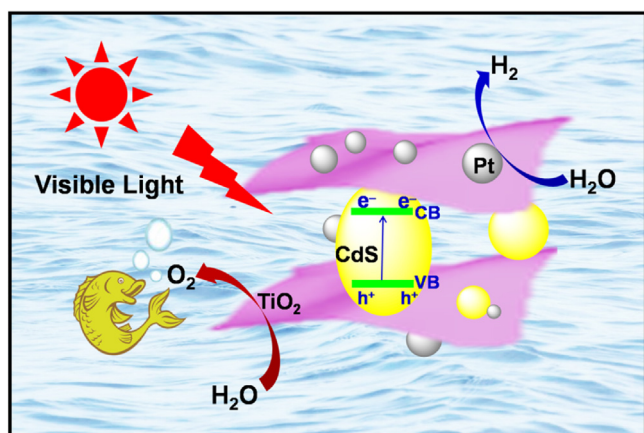
exhibited better photocatalytic H_2-production activity than CdS, and the sample of 2.0% Pt-(0.3 wt%)TiO_2/CdS had the best activity.

The stability of prepared CdS based photocatalysts were further clarified by cyclic experiments. Four successive runs were conducted without renewing the photocatalyst, and the corresponding results were displayed in Fig. 10. It displayed that the CdS sample itself showed a low and gradually decreased performance during the repeating photocatalytic reactions. When the CdS surface was covered by TiO_2 thin film, TiO_2/CdS exhibited a higher stability toward photocatalytic H_2-evolution performance. It was because the photogenerated holes on the VB of CdS would first transfer to

Scheme 2. The mechanism of overall water splitting over Pt-TiO$_2$/CdS under visible illumination and artificial gill.

Fig. 12. The concentration of Cd^{2+} for each run in the reaction solution of CdS and Pt-TiO$_2$/CdS under visible light irradiation with artificial gill.

the TiO$_2$ thin film, instead of oxidation S^{2-} in CdS. Furthermore, after modification Pt cocatalyst on TiO$_2$/CdS surface, its photocatalytic activity and stability were further enhanced compared with the CdS and TiO$_2$/CdS samples. Here the Pt nanoparticle cocatalysts served as both effective capture site to accept the photogenerated electrons and the reduction active site to promote the interfacial H$_2$-evolution reactions, meanwhile. The TiO$_2$ thin film could inhibit photocorrosion of CdS. The mechanism of H$_2$ evolution over the Pt-TiO$_2$/CdS catalyst under visible illumination was depicted in Scheme 2.

Clearly, Pt-TiO$_2$/CdS photocatalyst showed comparatively low activity in the absence of artificial gill, its stability was low as well. The artificial gill not only remove newly formed O$_2$ from water to prevent the oxygen leading photocorrosion, but probably inhibit the hydrogen and oxygen back recombination to water.

To investigate the wavelength dependence of photocatalytic H$_2$ evolution, the AQE of Pt-TiO$_2$/CdS for hydrogen evolution was examined over a wide visible light range of 430–550 nm. As shown in Fig. 11, it can be seen that the AQE decreases with increasing wavelengths. The highest AQE of Pt-TiO$_2$/CdS photocatalytic overall water splitting system was 0.17% at 430 nm.

It is known that CdS photocorrosion is due to the sulfide oxidation, and that kind oxidation could be triggered by photogenerated hole or newly formed oxygen in the dispersion solution. When the CdS was photocorroded, the Cd^{2+} would be released into the dispersion solution. One can check the photocorrosion degree of
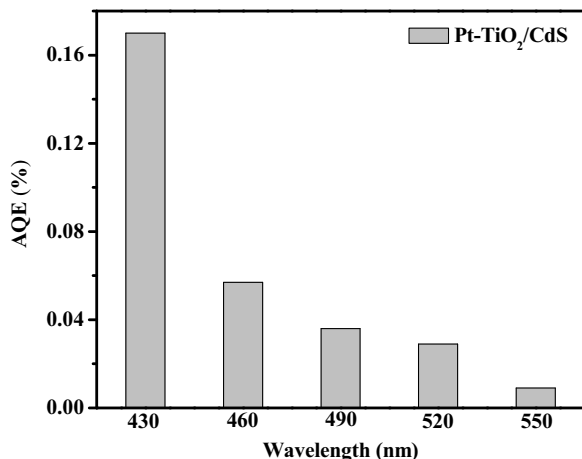
catalyst by measurement of the concentration of Cd^{2+} in the reaction solution after reaction. To clarify the photocorrosion degree of various CdS catalysts, ICP analysis of Cd^{2+} concentration in the reaction solutions for each run was carried out. As displayed in Fig. 12, it was clear that the concentration of Cd^{2+} had a gradual rise with the increasing irradiation time for CdS itself, indicating the CdS photocorrosion. But there was only negligible Cd^{2+} in the Pt-TiO$_2$/CdS dispersion after several cycles, far below than that of CdS sample. The result was well agreement with the photocatalytic performance, implied that excellent photocatalytic performance of Pt-TiO$_2$/CdS owing to its efficient inhibition of photocorrosion.

In addition, in order to check the change in the bulk and surface composition after the photocatalytic H$_2$ evolution, the phase structures were also characterized by XRD and XPS technologies after repeating photocatalytic reaction. As shown in Fig. S2 (XRD), Fig. S3 (XPS), Fig. S4 (SEM) and Table S1 of the element component analysis based on the XPS results, it is clear that the main phase structure and surface microstructures of different CdS-based catalysts remained unchanged before and after repeated photocatalytic reactions. As shown in Fig. 13, however, a small amount of S^0 was observed except the S^{2-} in CdS. That probably corresponded weak deactivation of CdS catalyst after recycling photocatalytic tests, and could be ascribed to its photoinduced instability. The ratio of S^0/S(total)

Fig. 11. Apparent quantum efficiencies (AQE) of H$_2$ evolution for by Pt-TiO$_2$/CdS under light irradiation with different wavelengths. Irradiation time: 2 h.
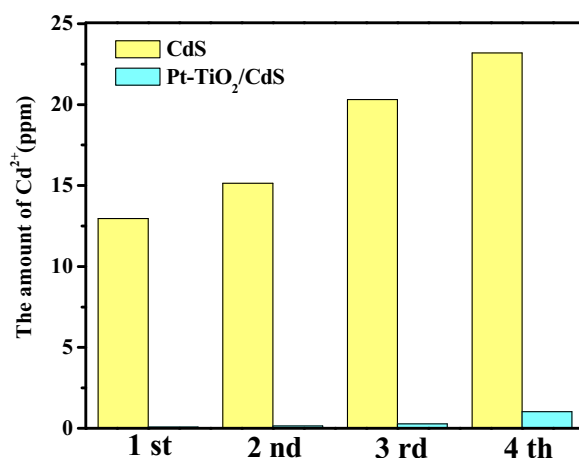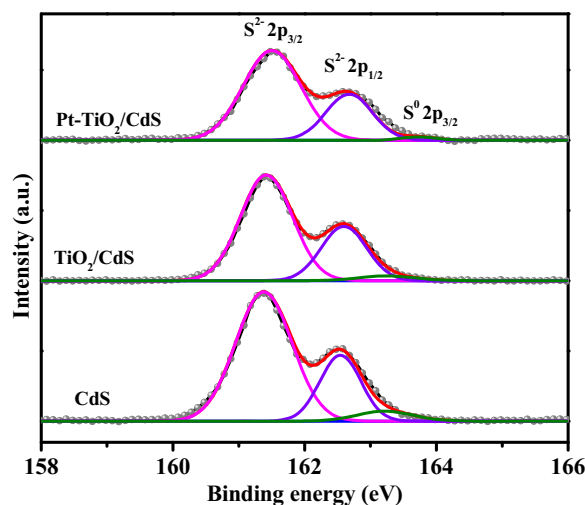

Fig. 13. High-resolution XPS spectra of S 2p for the various samples after photocatalytic reactions: CdS, TiO$_2$/CdS and Pt-TiO$_2$/CdS.
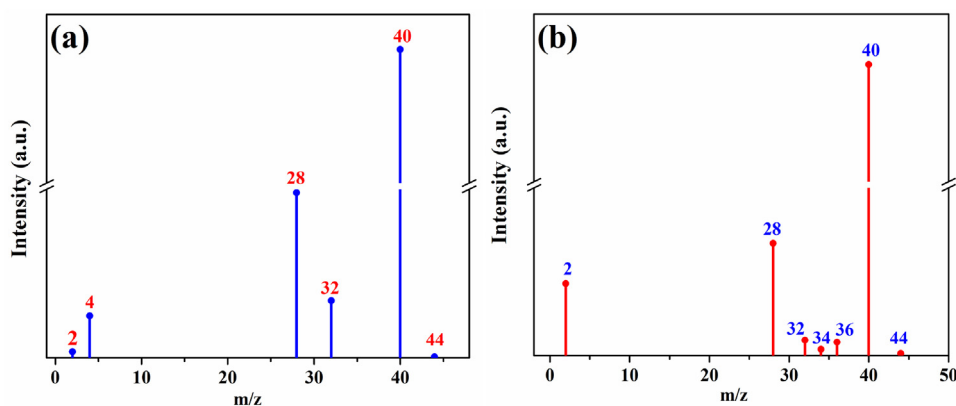
Fig. 14. GC–MS spectra of the gas phase species produced during illumination 6 h toward photocatalytic splitting (a) D_2O, (b) $H_2{}^{18}O$.

was about 5.26 at% for CdS itself, while S^0/S(total) was 1.49 at% only after surface modification by TiO_2 thin film. When Pt was loaded on the TiO_2/CdS surface, formation S^0 (S^0/S(total) = 0.58%) was rarely detected, indicating TiO_2 and Pt loading could inhibit the deactivation of CdS. Those results confirmed the photoreaction stability of CdS could be greatly improved by TiO_2 thin film, Pt loading and application of artificially gill.

To further certify that Pt-TiO_2/CdS catalyst could achieve overall water splitting under visible light irradiation, the isotopes tracer experiments were performed and the results were shown in Fig. 14. The gases were analyzed by GC–MS. In Fig. 14a, the isotopes analysis results illustrated the m/z signal at 4, corresponding to the D_2. The results of photocatalytic splitting $H_2{}^{18}O$ displayed in Fig. 14b, the m/z signal at 36 corresponded to the $^{18}O_2$, while the m/z of 2, 28, 32, 34, 40 and 44 corresponded to the trace amount of H_2, N_2, O_2, ^{18}O–O, Ar and CO_2. The detected $^{18}O_2$ confirmed that formed oxygen was from $H_2{}^{18}O$. The both isotopes tracer experiments prove that Pt-TiO_2/CdS photocatalyst is able to overall water splitting.

A series of comparative analysis of photoelectrochemical and photoluminescence (PL) spectra on CdS, TiO_2/CdS and Pt-TiO_2/CdS

samples were carried out. Fig. 15A shows the transient photocurrent response of the CdS, TiO_2/CdS and Pt-TiO_2/CdS over several on-off cycles of visible light irradiation. The anodic photocurrent produced by the visible light irradiation was observed with good reproducibility in all samples. The initial anodic photocurrent under visible light irradiation originates from the efficient separation of photogenerated electrons and holes. The photoinduced electrons or holes can subsequently cause the reduction or oxidation reaction with water or oxygen molecules absorbed on the surface of Pt-TiO_2/CdS [87]. The photocurrent value of the Pt-TiO_2/CdS was two times higher than that of pure CdS, indicating the separation efficiency of the photogenerated electrons and holes have been greatly enhanced by the synergistic effect of TiO_2 as a hole cocatalyst and Pt as an electron cocatalyst. Moreover, there was a sharp attenuation of the photocurrent when the light was off. Fig. 15B displayed the variation of current with applied bias voltage, where it was clear to see that current of the samples increased with the forward bias voltage, indicative of typical n-type semiconductor behavior of catalyst [88]. The observed cathodic current can be ascribed to the H_2 formation in the range of 0 to −1.0 V
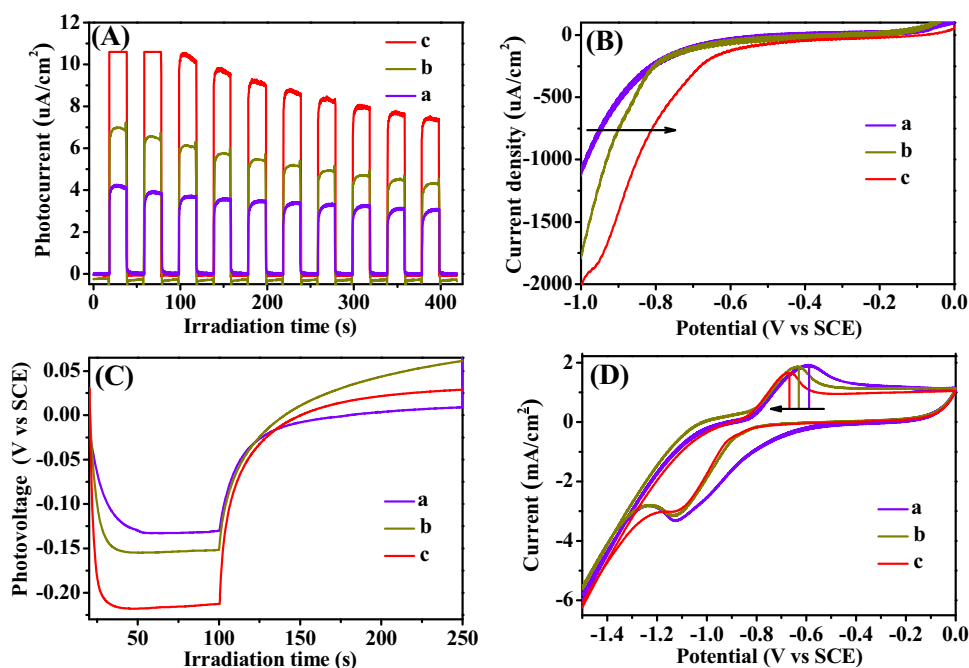

Fig. 15. (A) Transient photocurrent responses, (B) linear-sweep voltammograms collected with a scan rate of 1 mV/s, and (C) Illuminated open circuit potential and (D) cyclic voltammograms of (a) CdS, (b) TiO_2/CdS and (c) Pt-TiO_2/CdS composites.
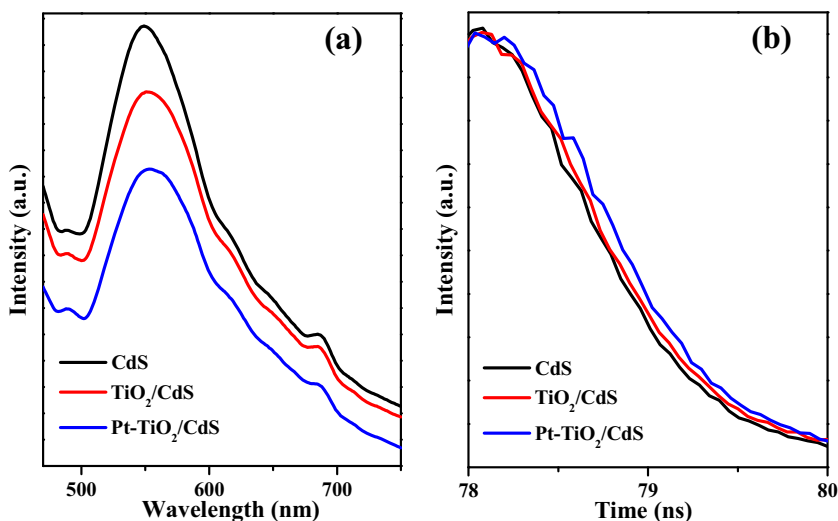
Fig. 16. (a) Photoluminescence (PL) spectra and (b) Time-resolved fluorescence decays of the as-synthesized samples with an excitation wavelength of 425 nm.

Table 2
Fluorescence lifetimes of CdS, TiO_2/CdS and TiO_2/CdS samples.

Samples	Lifetime (ns)	Pre-exponential Factors B	Average lifetime (ns)	χ^2
CdS	$\tau_1 = 0.0414$ $\tau_2 = 0.0420$	$B_1 = 49.68$ $B_2 = 50.32$	0.042	1.022
TiO_2/CdS	$\tau_1 = 3.916$ $\tau_2 = 0.164$	$B_1 = 1.59$ $B_2 = 98.41$	1.203	1.111
Pt-TiO_2/CdS	$\tau_1 = 4.430$ $\tau_2 = 0.141$	$B_1 = 1.71$ $B_2 = 98.29$	1.657	1.022

versus SCE. Compared with pure CdS and TiO_2/CdS, Pt-TiO_2/CdS sample displayed an enhanced current. The results indicated that Pt-TiO_2/CdS possessed lower over-potential. Because the photocatalytic activity of hydrogen evolution was highly dependent on the over-potential HER reaction [89], Pt-TiO_2/CdS could possesses a better activity for hydrogen evolution. The open-circuit photovoltage (OCPV) technique can be utilized to assess the lifetime of photoelectrons and evaluate the efficiency seperation rate of the photogenerated electron-hole charge carriers [90,91]. Fig. 15C shows a typical OCPV responding to illumination followed by a break stop. Band gap excitation of CdS leads to charge separation, the electrons begin accumulating within the CdS. Electron accumulation makes a shift of the Fermi level to more negative potentials, therefore there is an increase of V_{oc}. The open-circuit voltage reaches a maximum as the electron accumulation competing with the charge recombination. Upon stop of illumination, V_{oc} decays as the electrons accumulated are scavenged by the electron acceptor species in the electrolyte as well as undergo recombination with trapped holes. The Pt-TiO_2/CdS nanocomposites show significant enhanced V_{oc} responses as compared to CdS and TiO_2/CdS, which suggests more efficient separation and transfer of photo-excited electron–hole pairs over Pt-TiO_2/CdS. Fig. 15D shows the cyclic voltammograms (CV) of CdS-based composites with obvious anodic and cathodic peaks for each sample. The oxidative potential −0.69 V (vs. SCE) of Pt-TiO_2/CdS corresponding to $E_{S^{2-}/S}$ was the most negative than that of TiO_2/CdS(−0.64 V (vs. SCE)) and CdS(−0.59 V (vs. SCE)). These results implied that S atom was effective protected from oxidation in Pt-TiO_2/CdS, which was well agreement with low Cd^{2+} concentration in the reaction solution, thus a thin TiO_2 film on the CdS surface could prohibit the photocorrosion.

To gain insight into the separation and recombination between photogenerated electrons and holes, the photoluminescence (PL) spectrum was carried out [92,93]. As depicted in Fig. 16a, after

the modification of TiO_2 thin film and metal Pt, the PL intensity of Pt-TiO_2/CdS composites was diminished compared to that of pure CdS and TiO_2/CdS, which was due to the trap or shuttle the photogenerated electrons to metal Pt, thus retarding the undesirable recombination process of the electron-hole pairs. The results of time-resolved PL spectroscopy were shown in Fig. 16b and Table 2, the average lifetime of the samples increased in the order of CdS< TiO_2/CdS < Pt-TiO_2/CdS, which could be explained by the effect of efficiently expediting the migration of charge carriers and inhibit the electron-hole recombination by TiO_2 thin film and Pt nanoparticle, thus lifetime of charge carriers was prolonged. Both photoelectrochemical and PL experiments confirmed the synergetic effect of TiO_2 film and Pt loading, which could boost the separation and transfer of the photogenerated electrons and eventually resulted in the higher photocatalytic efficiency of Pt-TiO_2/CdS than that of CdS and TiO_2/CdS toward H_2 evolution under visible light illumination.

4. Conclusions

In summary, TiO_2 film and Pt nanoparticle were successfully loaded on the CdS surface by a facile impregnation method at room temperature. After modification, CdS exhibited an obviously enhanced photocatalytic activity and stability, which attributed to the synergistic effects of TiO_2 thin film and Pt nanoparticle. The TiO_2 film as hole-cocatalyst can effectively protect CdS from photocorrosion by rapidly transferring the interfacial photogenerated holes, the metal Pt nanoparticle as electron-cocatalyst can rapidly capture the photogenerated electrons and then function as the reduction active site to promote the interfacial H_2-evolution reaction. Furthermore, the application of artificial gill in photocatalytic overall water splitting could remove newly formed O_2 from water to prevent the oxygen leading photocorrosion and to inhibit the hydrogen

and oxygen recombination back to water. By these two strategies, we could fulfill visible light induced overall water splitting by CdS and achieved satisfied stability during reaction. This work may provide new insight for the development of highly stable and efficient photocatalysts in sulfide semiconductor dispersion for hydrogen production.

Acknowledgments

Appendix A. Supplementary data

Supplementary data associated with this article can be found, in the online version, at http://dx.doi.org/10.1016/j.apcatb.2017.04.074.

References

[1] Q. Zhang, Z. Li, S. Wang, R. Li, X. Zhang, Z. Liang, H. Han, S. Liao, C. Li, ACS Catal. 6 (2016) 2182–2191.
[2] H. Gao, W. Zhen, J. Ma, G.X. Lu, Appl. Catal. B 206 (2017) 353–363.
[3] Z. Li, B. Tian, W. Zhang, X. Zhang, Y. Wu, G.X. Lu, Appl. Catal. B 204 (2017) 33–42.
[4] W. Wang, G.X. Lu, Prog. Chem. 15 (2003) 74–78.
[5] G.X. Lu, S.B. Li, Int. J. Hydrogen Energy 17 (1992) 767–770.
[6] A. Kudo, Y. Miseki, Chem. Soc. Rev. 38 (2009) 253–278.
[7] G.X. Lu, H. Gao, J. Suo, S.B. Li, J. Chem. Soc. Chem. Commun. 21 (1994) 2423–2424.
[8] Z. Li, B. Tian, W. Zhen, Y. Wu, G.X. Lu, Appl. Catal. B 203 (2017) 408–415.
[9] B. Tian, W. Zhen, H. Gao, X. Zhang, Z. Li, G.X. Lu, Appl. Catal. B 203 (2017) 789–797.
[10] W. Zhen, F. Gao, B. Tian, P. Ding, Y. Deng, H. Gao, G.X. Lu, J. Catal. 348 (2017) 200–211.
[11] X. Zhang, G.X. Lu, Carbon 108 (2016) 215–224.
[12] K. Maeda, K. Teramura, D. Lu, N. Saito, Y. Inoue, K. Domen, Angew. Chem. 118 (2006) 7970–7973.
[13] K. Maeda, K. Domen, J. Phys. Chem. Lett. 1 (2010) 2655–2661.
[14] Y. Sasaki, A. Iwase, H. Kato, A. Kudo, J. Catal. 259 (2008) 133–137.
[15] X. Zhao, G.X. Lu, Int. J. Hydrogen Energy 41 (2016) 13993–14002.
[16] W. Zhen, J. Ma, G.X. Lu, Appl. Catal. B 190 (2016) 12–25.
[17] Z. Li, Y. Wu, G.X. Lu, Appl. Catal. B 188 (2016) 56–64.
[18] W. Zhen, H. Gao, B. Tian, G.X. Lu, ACS Appl. Mater. Interface 8 (2016) 10808–10819.
[19] Y. Guo, G.X. Lu, Int. J. Hydrogen Energy 41 (2016) 6706–6712.
[20] B. Tian, Z. Li, W. Zhen, G.X. Lu, J. Phys. Chem. C 120 (2016) 6409–6415.
[21] X. Zhao, G.X. Lu, Int. J. Hydrogen Energy 41 (2016) 3349–3362.
[22] Y. Inoue, Energ. Environ. Sci. 2 (2009) 364–386.
[23] Y. Wu, G.X. Lu, Phys. Chem. Chem. Phys. 16 (2014) 4165–4175.
[24] Y. Wu, G.X. Lu, S.B. Li, J. Photochem. Photobiol. A Chem. 181 (2006) 263–267.
[25] N. Arai, N. Saito, H. Nishiyama, Y. Inoue, K. Domen, K. Sato, Chem. Lett. 35 (2006) 796–797.
[26] L. Li, Y. Huang, A. Zhang, M. Xiang, J. Yang, M. Jiao, J. Mol. Catal. (China) 30 (2016) 470–479.
[27] Z. Zou, J. Ye, K. Sayama, H. Arakawa, Nature 414 (2001) 625–627.
[28] W. Zhang, G.X. Lu, Catal. Sci. Technol. 6 (2016) 7693–7697.
[29] W. Zhang, C. Kong, W. Gao, G.X. Lu, Chem. Commun. 52 (2016) 3038–3041.
[30] K. Maeda, T. Takata, M. Hara, N. Saito, Y. Inoue, H. Kobayashi, K. Domen, J. Am. Chem. Soc. 127 (2005) 8286–8287.
[31] C. Li, Z. Lei, Q. Wang, F. Cao, F. Wang, W. Shanguan, J. Mol. Catal. (China) 29 (2015) 381–389.
[32] K.G. Kanade, J.-O. Baeg, B.B. Kale, S.M. Lee, S.-J. Moon, K.-j. Kong, Int. J. Hydrogen Energy 32 (2007) 4678–4684.
[33] Z. Li, C. Kong, G.X. Lu, J. Phys. Chem. C 120 (2016) 56–63.
[34] Z. Li, Q. Wang, C. Kong, G.X. Lu, J. Phys. Chem. C 119 (2015) 13561–13568.
[35] G. Hitoki, T. Takata, J.N. Kondo, M. Hara, H. Kobayashi, K. Domen, Chem. Commun. 16 (2002) 1698–1699.
[36] W. Wang, T.W. Ng, W.K. Ho, J. Huang, S. Liang, T. An, G. Li, J.C. Yu, P.K. Wong, Appl. Catal. B 129 (2013) 482–490.
[37] W. Zhen, B. Li, G.X. Lu, Chem. Commun. 51 (2015) 1728–1731.
[38] C. Kong, S. Min, G.X. Lu, Chem. Commun. 50 (2014) 9281–9283.
[39] E. Cui, G.X. Lu, Int. J. Hydrogen Energy 39 (2014) 7672–7685.
[40] C. Kong, S. Min, G.X. Lu, ACS Catal. 4 (2014) 2763–2769.
[41] D.P. Kumar, S. Hong, D.A. Reddy, T.K. Kim, J. Mater. Chem. A 4 (2016) 18551–18558.
[42] X. Zong, H. Yan, G. Wu, G. Ma, F. Wen, L. Wang, C. Li, J. Am. Chem. Soc. 130 (2008) 7176–7177.
[43] F. Ma, Y. Wu, Y. Shao, Y. Zhong, J. Lv, X. Hao, Nano Energy 27 (2016) 466–474.
[44] P. He, Y. Chen, W. Fu, J. Mol. Catal. (China) 30 (2016) 269–275.
[45] C. Kong, Z. Li, G.X. Lu, Int. J. Hydrogen Energy 40 (2015) 9634–9641.
[46] Z. Li, C. Kong, G.X. Lu, Int. J. Hydrogen Energy 40 (2015) 9061–9068.
[47] C. Kong, Z. Li, G.X. Lu, Int. J. Hydrogen Energy 40 (2015) 5824–5830.
[48] C. Kong, S. Min, G.X. Lu, Int. J. Hydrogen Energy 39 (2014) 4836–4844.
[49] C. Kong, S. Min, G.X. Lu, Chem. Commun. 50 (2014) 5037–5039.
[50] X. Zhang, Z. Jin, Y. Li, G.X. Lu, J. Power Source 166 (2007) 74–79.
[51] B. Li, W. Zhen, G. Lu, J. Ma, J. Mol. Catal. (China) 29 (2015) 152–163.
[52] E. Cui, G.X. Lu, Int. J. Hydrogen Energy 39 (2014) 8959–8968.
[53] G. Zhang, Z.-A. Lan, X. Wang, Angew. Chem. Int. Ed. 55 (2016) 15712–15727.
[54] Z. Pan, Y. Zheng, F. Guo, P. Niu, X. Wang, ChemSusChem 10 (2017) 87–90.
[55] J. Ni, X. Luo, Y. Zhan, J. Lin, J. Mol. Catal. (China) 30 (2016) 282–296.
[56] D.N. Ke, S.L. Liu, K. Dai, J.P. Zhou, L.N. Zhang, T.Y. Peng, J. Phys. Chem. C 113 (2009) 16021–16026.
[57] G. Lu, S. Zhang, G. Hou, F. Shi, T. Li, X. Yao, H. Liang, J. Mol. Catal. (China) 30 (2016) 383–390.
[58] J. Ran, J. Zhang, J. Yu, M. Jaroniec, S.Z. Qiao, Chem. Soc. Rev. 43 (2014) 7787–7812.
[59] D. Jing, L. Guo, J. Phys. Chem. B 110 (2006) 11139–11145.
[60] D.J. Fermín, E.A. Ponomarev, L.M. Peter, J. Electroanal. Chem. 473 (1999) 192–203.
[61] N.M. Dimitrijevic, S. Li, M. Grätzel, J. Am. Chem. Soc. 106 (1984) 6565–6569.
[62] S. Zhang, Q. Chen, D. Jing, Y. Wang, L. Guo, Int. J. Hydrogen Energy 37 (2012) 791–796.
[63] C. Wang, L. Wang, J. Jin, J. Liu, Y. Li, M. Wu, L. Chen, B. Wang, X. Yang, B.-L. Su, Appl. Catal. B 188 (2016) 351–359.
[64] Y. Hu, X. Gao, L. Yu, Y. Wang, J. Ning, S. Xu, X.W. Lou, Angew. Chem. 125 (2013) 5746–5749.
[65] K. Li, M. Han, R. Chen, S.-L. Li, S.-L. Xie, C. Mao, X. Bu, X.-L. Cao, L.-Z. Dong, P. Feng, Y.-Q. Lan, Adv. Mater. 28 (2016) 8906–8911.
[66] Z. Sun, H. Zheng, J. Li, P. Du, Energy Environ. Sci. 8 (2015) 2668–2676.
[67] E. Lalik, A. Drelinkiewicz, R. Kosydar, W. Rojek, T. Machej, J. Gurgul, T. Szumełda, M. Kołodziej, E. Bielanska, Int. J. Hydrogen Energy 40 (2015) 16127–16136.
[68] Y. Li, T. Tang, S. Peng, Z. Li, G.X. Lu, CrystEngComm 14 (2012) 6974–6982.
[69] X. Yue, X. Yi, R. Wang, Z. Zhang, S. Qiu, Nanoscale 8 (2016) 17516–17523.
[70] X. Ning, S. Meng, X. Fu, X. Ye, S. Chen, Green Chem. 18 (2016) 3628–3639.
[71] O.G. Holmes, D.S. McClure, J. Chem. Phys. 26 (1957) 1686–1694.
[72] H.G. Yu, H. Irie, Y. Shimodaira, Y. Hosogi, Y. Kuroda, M. Miyauchi, K. Hashimoto, J. Phys. Chem. C 114 (2010) 16481–16487.
[73] J. Tauc, R. Grigorovici, A. Vancu, Phys. Status Solidi B 15 (1966) 627–637.
[74] L. Nie, A. Meng, J. Yu, M. Jaroniec, Sci. Rep. 3 (2013) 3215.
[75] K.S.W. Sing, D.H. Everett, R.A.W. Haul, L. Moscou, R.A. Pierotti, J. Rouquérol, T. Siemieniewska, Pure Appl. Chem. 57 (1985) 603–619.
[76] J. Yu, S. Liu, H. Yu, J. Catal. 249 (2007) 59–66.
[77] W. Wang, J. Yu, Q. Xiang, B. Cheng, Appl. Catal. B 119–120 (2012) 109–116.
[78] M. Zhou, J. Yu, B. Cheng, J. Hazard. Mater. 137 (2006) 1838–1847.
[79] D.-H. Wang, L. Wang, A.-W. Xu, Nanoscale 4 (2012) 2046–2053.
[80] H. Zhao, Y. Dong, P. Jiang, G. Wang, H. Miao, R. Wu, L. Kong, J. Zhang, C. Zhang, ACS Sustain. Chem. Eng. 3 (2015) 969–977.
[81] Q. Wang, J. Li, Y. Bai, J. Lian, H. Huang, Z. Li, Z. Lei, W. Shangguan, Green Chem. 16 (2014) 2728–2735.
[82] P. Wang, T. Jiang, C. Zhu, Y. Zhai, D. Wang, S.J. Dong, Nano Res. 3 (2010) 794–799.
[83] A. Cao, Z. Liu, S. Chu, M. Wu, Z. Ye, Z. Cai, Y. Chang, S. Wang, Q. Gong, Y. Liu, Adv. Mater. 22 (2010) 103–106.
[84] S. Hoang, S.P. Berglund, N.T. Hahn, A.J. Bard, C.B. Mullins, J. Am. Chem. Soc. 134 (2012) 3659–3662.
[85] H. Yu, G. Cao, F. Chen, X. Wang, J. Yu, M. Lei, Appl. Catal. B 160 (2014) 658–665.
[86] X. Jiang, X. Fu, L. Zhang, S. Meng, S. Chen, J. Mater. Chem. A 3 (2015) 2271–2282.
[87] X.T. Pian, B.Z. Lin, Y.L. Chen, J.D. Kuang, K.Z. Zhang, L.M. Fu, J. Phys. Chem. C 115 (2011) 6531–6539.
[88] M.J. Natan, J.W. Thackeray, M.S. Wrighton, J. Phys. Chem. 90 (1986) 4089–4098.
[89] Y. Li, D. Gao, S. Peng, G. Lu, S. Li, Int. J. Hydrogen Energy 36 (2011) 4291–4297.
[90] F.-X. Xiao, S.-F. Hung, J. Miao, H.-Y. Wang, H. Yang, B. Liu, Small 11 (2015) 554–567.
[91] Benjamin H. Meekins, Prashant V. Kamat, ACS Nano 3 (2009) 3437–3446.
[92] N. Zhang, Y.-J. Xu, Chem. Mater. 25 (2013) 1979–1988.
[93] N. Zhang, M.-Q. Yang, Z.-R. Tang, Y.-J. Xu, ACS Nano 8 (2014) 623–633.